JOURNAL OF MATERIALS SCIENCE 33 (1998) 3639–3649

Liquid separation in Cu–Co and Cu–Co–Fe alloys solidified at high cooling rates

A. MUNITZ
Nuclear Research Center–Negev, PO Box 9001, Beer-Sheva, Israel

R. ABBASCHIAN
Department of Materials Science and Engineering, University of Florida, Gainesville, FL 32611, USA

The impact of cooling rates on the microstructure of Cu–Co and Cu–Fe–Co alloys was investigated by scanning electron microscopy. The high cooling rates entailed in the electron beam surface melting of the alloys result in bulk supercooling of at least 150 K, which in turn causes three microstructural effects: (i) melt separation into two liquids, namely copper poor, L1, and copper rich, L2; (ii) microstructural refinement; (iii) enhanced solute trapping of Cu in the Fe- or Co-rich phases. No evidence of metastable liquid separation was found for Cu–50 wt % Co. There are indications that similar dynamic supercooling exists in copper-quenched or arc-melted samples near the splat contact.

1. Introduction

Rapid solidification processing (RSP) might affect several alloy properties such as microstructural refinement [1, 2], extension of solid solubilities [3] or formation of non-equilibrium phases [1, 4]. This, in turn, may improve the strength, increase plasticity, extend fatigue life, enhance stress corrosion resistance and affect some other related properties of alloys [1]. The extension of solid solubility of alloys exhibiting metastable miscibility gap, such as Cu–Co alloys, has recently attracted much interest because of the appearance of giant magnetoresistance (GMR) effects [5–8], namely a large drop in the electrical resistance, R, in response to an applied magnetic field. For example, thermal annealing of supersaturated of $Cu_{90}Co_{10}$ solid solution at 440 °C reveals an increased magnetoresistance of up to 11% at room temperature. It is believed that the heat treatment caused solid-state spinodal decomposition, which is responsible for the changes in magnetoresistance.

It has been argued that high cooling rates might result in a considerable dynamic bulk supercooling even in thick (larger than 100 μm) specimens [9, 10]. For example, 282 K supercooling was achieved for Al–6.9 wt % Mn solidified at cooling rates of 3×10^5 K s^{-1} [9]. Thermal calculations [11] have shown that the amount of supercooling that one may obtain when an aluminium layer 250 μm thickness is brought into good thermal contact with a massive copper substrate, initially at ambient temperature, is a function of the distance from the copper chill. For example, at a distance of 5 μm, one may obtain a decrease as high as 250 K relative to the pouring temperature, while the temperature decrease is only about 130 K at a distance of 50 μm. Therefore, solidification under high cooling rates, such as effected by electron beam surface melting or splat quenching of layers of thickness less than 1 mm on a copper plate, might also involve solidification under supercooling. The latter can result in diverse solidification modes such as partitionless (massive) solidification [12, 13] (in which the solid has the same concentration as the parent liquid) and/or melt separation [10, 14–16].

It has been recently shown that supercooling of Cu–Co or Cu–Fe alloys beyond a certain limit results in separation of the melt into two liquids; one is Cu rich (L2), and the other is, respectively, Co or Fe rich (L1) [14–18]. Moreover, our previous work on the microstructure of supercooled Cu–Co alloys showed the existence of a metastable Cu phase containing 13–20 wt % Co [10]. Large cooling rates of the order of 10^5 K s^{-1} during electron beam surface melting was also shown to cause bulk supercooling levels of about 150 K, in turn causing melt separation. Similar melt separation was also observed in Cu–Fe alloys [16].

The present work was aimed at obtaining better understanding of the impact of high cooling rates on the microstructure of Cu–Co and Cu–Fe–Co systems.

2. Experimental procedures

High-purity (99.98%) copper, high-purity (99.99%) iron, and high-purity (99.99%) cobalt were used to prepare Cu–Co alloys containing up to 80 wt % Co and ternary Cu–Fe–Co alloys of various compositions, as listed in Table I. Specimens of the desired compositions were arc melted using a non-consumable tungsten electrode, followed by electron beam

TABLE I Alloy compositions and the resulting microstructures

Sample number	Composition			Microstructural observation	
	Cu (wt %)	Fe (wt %)	Co (wt %)	Arc melting	Electron beam surface melting
Cu–Co) 1	90	10	—	Dendritic	Melt separation
Cu–Co) 2	70	30	—	Dendritic	Melt separation
Cu–Co) 3	50	50	—	Dendritic	Dendritic
Cu–Co) 4	20	80	—	Dendritic	Dendritic
Cu–Fe–Co) 1	90	5	5	Dendritic	Dendritic
Cu–Fe–Co) 2	85	15	5	Dendritic	Melt separation
Cu–Fe–Co) 3	75	15	10	Melt separation near splat; rest dendritic	Melt separation; tiny spheres
Cu–Fe–Co) 4	75	10	15	Melt separation near splat; rest dendritic	Melt separation; tiny spheres
Cu–Fe–Co) 5	70	15	15	Melt separation near splat; rest dendritic	Melt separation
Cu–Fe–Co) 6	65	20	15	Dendritic	Melt separation; small spheres
Cu–Fe–Co) 7	65	10	25	Dendritic	Melt separation; large spheres
Cu–Fe–Co) 8	60	20	20	Dendritic	Melt separation; large spheres
Cu–Fe–Co) 9	60	30	10	Dendritic	Melt separation; large spheres
Cu–Fe–Co) 10	15	30	15	Dendritic	Melt separation; large spheres
Cu–Fe–Co) 11	55	25	20	Dendritic	Melt separation; large spheres
Cu–Fe–Co) 12	50	25	25	Dendritic	Dendritic
Cu–Fe–Co) 13	45	40	15	Dendritic	Dendritic
Cu–Fe–Co) 14	40	40	20	Dendritic	Dendritic
Cu–Fe–Co) 15	30	40	30	Dendritic	Dendritic
Cu–Fe–Co) 16	20	60	20	Dendritic	Dendritic
Cu–Fe–Co) 17	20	40	40	Dendritic	Dendritic

surface melting. In order to obtain homogeneous samples, several remelting cycles were performed, with the specimens turned upside down before each remelting. The surface of processed samples were flattened by abrading one side with SiC papers (grade 600). Then, the surfaces were melted using an electron beam with a driving voltage of 60 kV, a current of between 4 and 10 mA, and a scanning velocity of about 5 m min^{-1}. The electron beam was focused to about 1 mm beneath the surface. The cooling rates achieved are estimated to be as high as 10^6 K s^{-1} [19, 20].

The Cu–Co alloys were also electromagnetically levitated and splat cooled from the superheated or supercooled state. The experimental procedure has been described elsewhere in detail [10]. It involved levitation of approximately 1.5 g samples in an inert-gas atmosphere, followed by freezing of the melt from a superheated or supercooled state on a copper chill plate.

After solidification, the samples were cross sectioned and prepared using standard metallographic procedures. The specimens were etched in a solution which consisted of 120 ml of H_2O, 10 g of ammonium cupric chloride and sufficient ammonium hydroxide to dissolve all the ammonium cupric chloride crystals. The etching time ranged between 5 and 12 s. The microstructures and compositional profiles were investigated using a scanning electron microscope with energy-dispersive spectroscopy (EDS) capabilities. For the EDS analysis, the specimens were etched only very lightly so as to reveal the microstructure, yet keeping the surface roughness to a minimum. The raw scanning electron microscopy (SEM) intensity data were corrected with a standard *ZAF* computer program [21].

3. Results

3.1. Electron beam surface melting of Cu–Co alloys

In Figs 1–4, secondary-electron images (SEIs) of various Cu–Co microstructures obtained after electron beam surface melting are presented. In Fig. 1a, a general view of the fusion zone in a Cu–10 wt % Co substrate is shown. The substrate, seen in the lower part of the micrograph, consisted of primary Co-rich dendrites embedded in a Cu-rich matrix. Some of the unmelted Co-rich dendrites are seen to protrude into the fused zone. However, about 10–20 μm above the fusion line, Co-rich bands are observed, which had an average Co-concentration of approximately 20 wt %, compared with the average alloy Co-concentration of only 10 wt %. These bands contained Co-rich spherulites with various sizes (Fig. 1c). Approximately 100 μm from the fusion line, the microstructure consisted of spherulites which covered the area uniformly, as shown in Fig. 1d. Similar microstructures were observed in a Cu–30 wt % Co alloy, as presented in

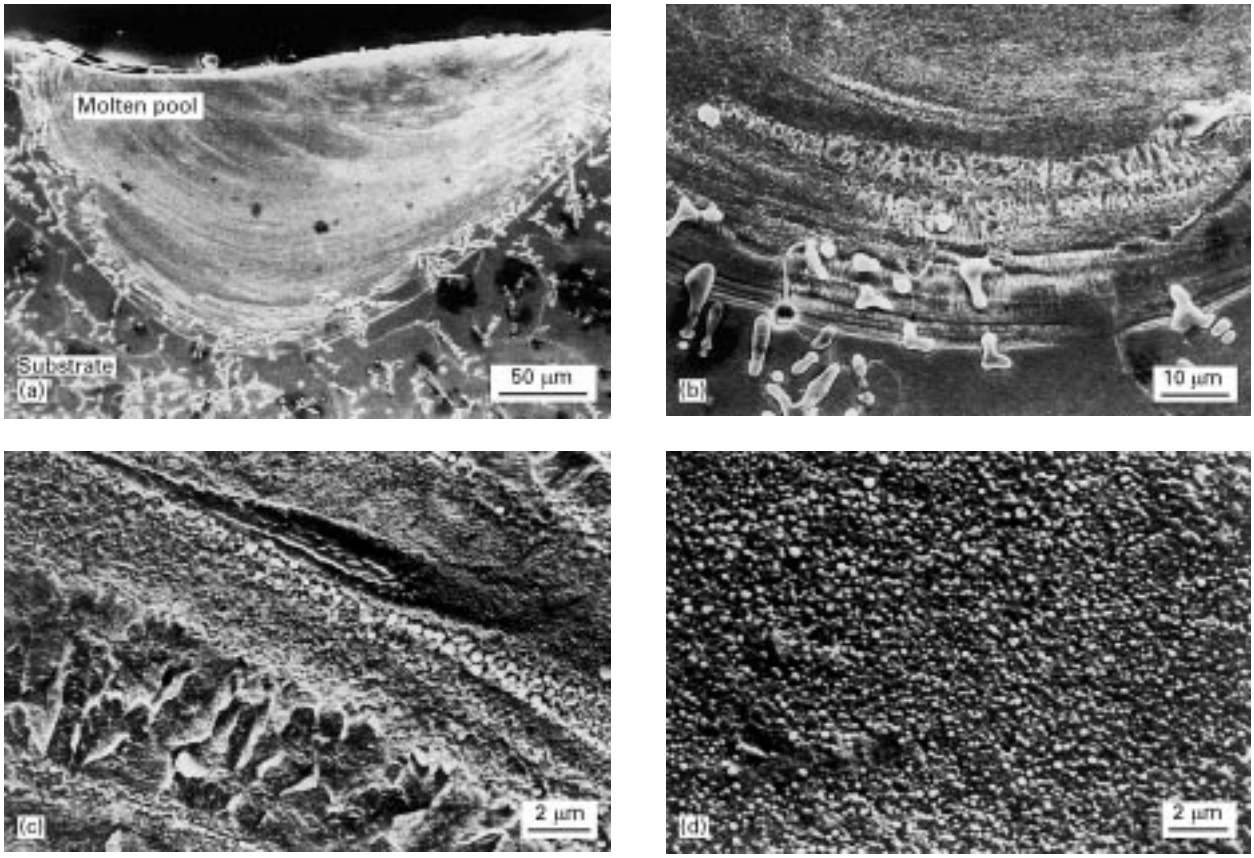

Figure 1 Secondary-electron images illustrating an electron beam melted zone of Cu–10 wt % Co: (a) an overall view; (b), (c) near the fusion line; (d) 100 μm away from the fusion line.

Fig. 2. The substrate (lower part of Fig. 2a and b) was similar to that shown in Fig. 1a and b, but with a larger volume fraction of Co dendrites. Three different morphological transitions were revealed near the fusion line, as shown in Fig. 2c and d. Initially, solidification started with a plane front mode, which changed to a cellular morphology about 15 μm away from the fusion line and eventually changed to dendritic. Beyond about 20 μm away from the fusion line, there is yet another morphological transition from dendritic to spherulitic, as can be seen in Fig. 2f. The latter region is similar to that shown in Fig. 2c.

The microstructure of an electron beam surface-melted Cu–50 wt % Co alloy is illustrated in Fig. 3. The general view of both the fused zone and its vicinity are given in Fig. 3a, with more detail shown in Fig. 3b and c. Up to 15 μm from the bottom of the fusion, a cellular structure was observed (Fig. 3b and c), which gradually changed to dendritic at about 50–70 μm away from the fusion line. The microstructure of the fusion line near the top of the molten pool is illustrated in Fig. 3d, where fine dendrites are observed instead of a cellular microstructure. After 150 μm away from the fusion line the microstructure was mixed cellular–dendritic, as seen in Fig. 3e. In contrast with the case of Cu–10–30 wt % Co alloys shown in Figs 1 and 2, no melt separation was observed in Cu–50 wt % Co alloys.

The microstructures of electron beam surface melting of a Cu–80 wt % Co alloy is illustrated in Fig. 4. The major effect of electron beam melting for this alloy is microstructural refinement, as can be seen from the variation in Fig. 4c.

3.2. Electron beam surface melting of Cu–Fe–Co alloys

Secondary-electron images (SEIs) illustrating the characteristic microstructure in the fused zone and its vicinity in Cu–Fe–Co specimens are presented in Figs 5 and 6. The microstructure of Cu–15 wt % Fe–10 wt % Co is illustrated in Fig. 5. The microstructure of the arc-melted specimen consisted of two regions (Fig. 5b): (i) up to 200 μm from the Cu chill the microstructure consisted of spherical particles with dendrites attached to them, or Co-rich dendrites embedded in a Cu-rich matrix (Fig. 5c); (ii) the rest of the sample contained primary Co-rich dendrites embedded in a Cu-rich matrix (Fig. 5d). The microstructure in the fused zone consisted of spheres embedded in a Cu-rich matrix. The spheres near the fusion line are smaller (Fig. 5e) than the spheres far from the fusion line (Fig. 5f). However, both spheres are at least one order of magnitude smaller than those observed in the arc melted samples.

Secondary-electron images illustrating the microstructure of Cu–20 wt % Fe–15 wt % Co are presented in Fig. 6. In Fig. 6a, a general view of the penetration of the fused zone into the substrate is shown. The substrate, which can be seen in the bottom of the micrograph, and in a larger magnification in Fig. 6b, consisted of primary Co-rich dendrites embedded in a Cu-rich matrix. The fusion line between the fused

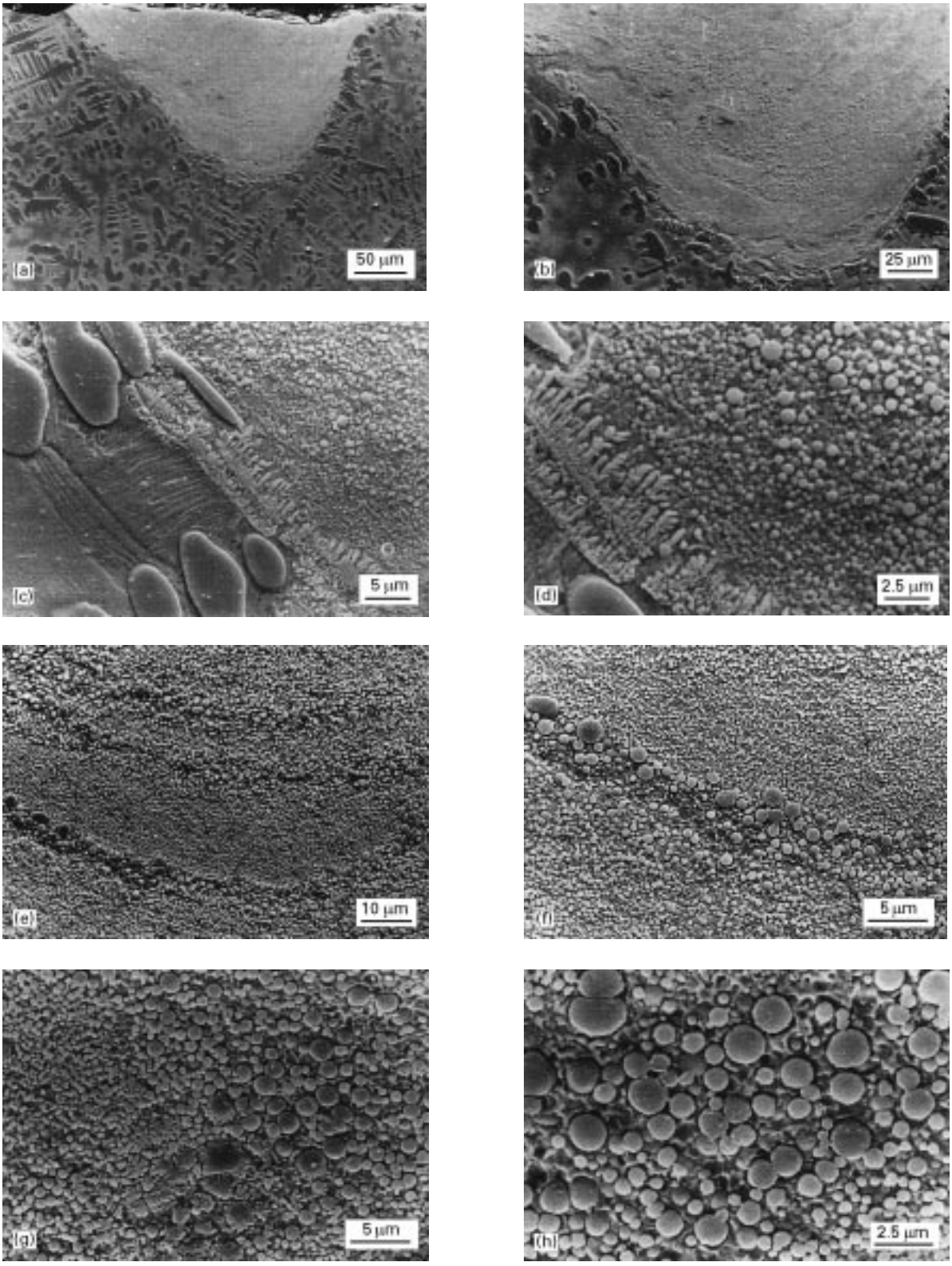

Figure 2 Secondary-electron images of an electron beam melted zone of a Cu–30 wt % Co alloy: (a), (b) an overall view; (c), (d) near the fusion line; (e), (f) enlargement of compositional bands; (g), (h) 100 μm from the fusion line.

zone and the matrix is shown in Fig. 6c. Unmelted primary dendrites are seen to protrude into the fused zone. It is reasonable to assume that only the Cu-rich matrix has been melted and then solidified epitaxially on the Cu-rich solid in the matrix. However, about 15 μm above the fusion line there is a morphology transition from a plane front solidification to a microstructure characteristic of solidification in the miscibility gap. In this case, the microstructure consisted of spherical particles which uniformly covered the area embedded in a copper matrix, as shown in Fig. 6d–f. The spherical particles are smaller than in the previous specimen. We attribute this change to the difference between the alloy compositions of the two specimens.

Secondary-electron images illustrating the characteristic melt separation microstructure in the fused zone as a function of Fe + Co concentration in the

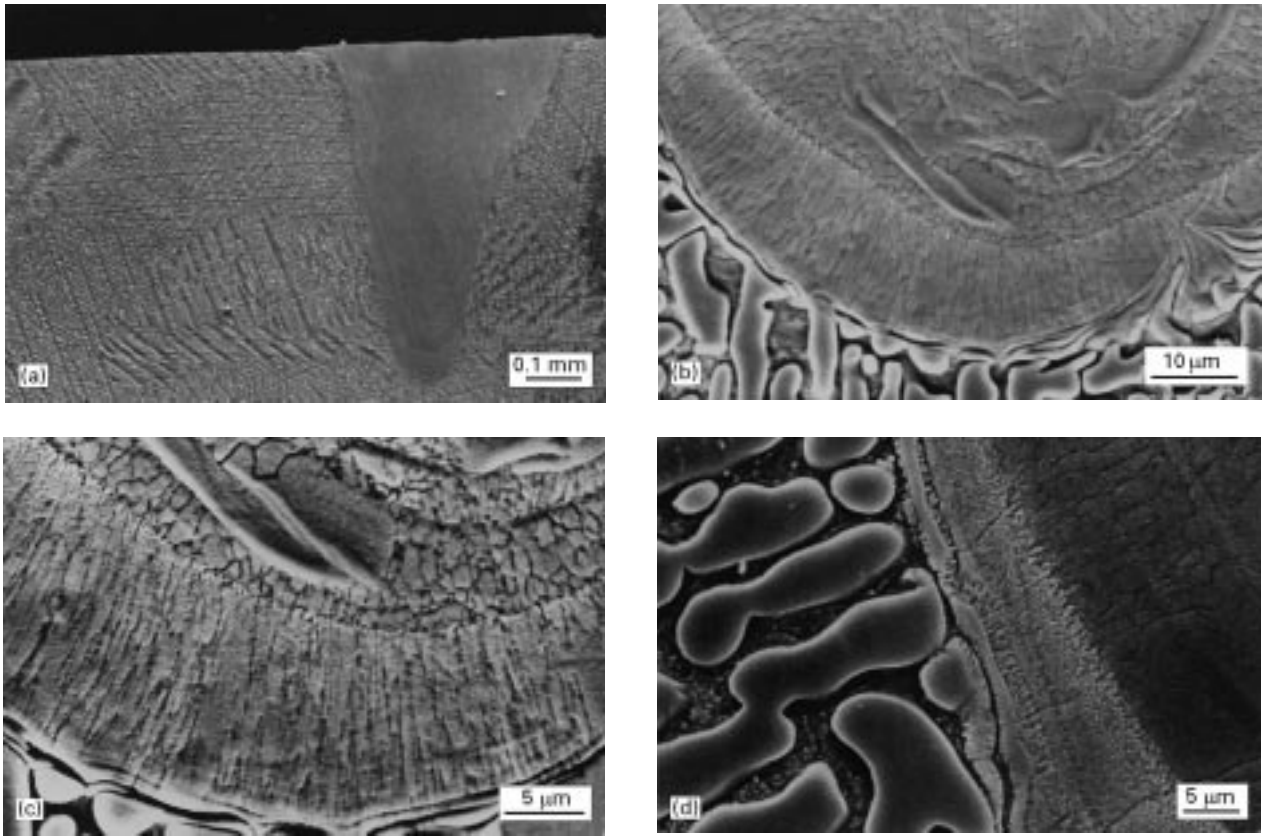

Figure 3 Secondary-electron images of an electron beam melted zone of Cu–50 wt % Co: (a) overall view of the substrate and the melted surface; (b), (c) near the fusion line at the maximum penetration depth; (d) near the fusion line at the molten pool top; (e) in the middle of the pool far away from the fusion line.

alloys are presented in Fig. 7. The microstructure of the fused zone depends on the alloy Co + Fe concentration. In alloys containing less than 45 wt % Fe + Co the microstructure consisted of spherical particles embedded in a Cu-rich matrix. The size of the spherulites depends on the Co + Fe content in the melt. At low values, the spherulites were small, as in Fig. 7a. Their size increased with increasing Fe + Co concentration in the melt (Fig. 7b and c). When the Fe + Co content was larger than 50 wt %, no melt separation could be observed. In those alloys a dendritic microstructure was observed.

3.3. Combined effects of supercooling and cooling rates on the microstructure

The combined effects of bulk supercooling and high cooling rates on the alloy microstructure are illustrated in Figs 8 and 9. In Fig. 8 secondary-electron images illustrating the microstructure of Cu–20 wt % Co alloys in regions near or far away from the copper chill surface are presented. Fig. 8a illustrates the microstructure about 40 μm away from the chill, of an alloy quenched from 90 K bulk supercooling. The estimated minimum supercooling required for this composition to enter the miscibility gap is about 150 K [10]. Nonetheless, one can see spherical particles, ranging from the submicron to about 3 μm in size. Another example, illustrating the same phenomenon, is presented in Fig. 8b–d for Cu–20 wt % Co specimens, supercooled to 160 K prior to quenching on the copper chill. The microstructure at a distance of about 10 μm distance from the copper chill (Fig. 8b) consisted of spherulites, about 1 μm in diameter, embedded in a matrix containing other finer spherulites. As solidification advances to about 60–80 μm from the chill (Fig. 8c and 8d), the L1 droplet size is seen to increase to about 3 μm. The growth of Co dendrites of the matrix (L2) emanating from the L1 particles (Fig. 8d) indicates that the L1 liquid solidified first.

A range of various microstructures was obtained across the splat samples, depending on the degree of supercooling and the samples geometry. Usually, the samples dropped on the copper chill were flat at the centre, becoming thicker towards their circumference. The microstructure of the thicker edge regions consisted of primary α-Co dendrites embedded in a peritectic ε-Cu matrix, similar to that shown in Fig. 9f. On the other hand, the microstructure in the flat region depended on its thickness, *D*. For thicknesses up to

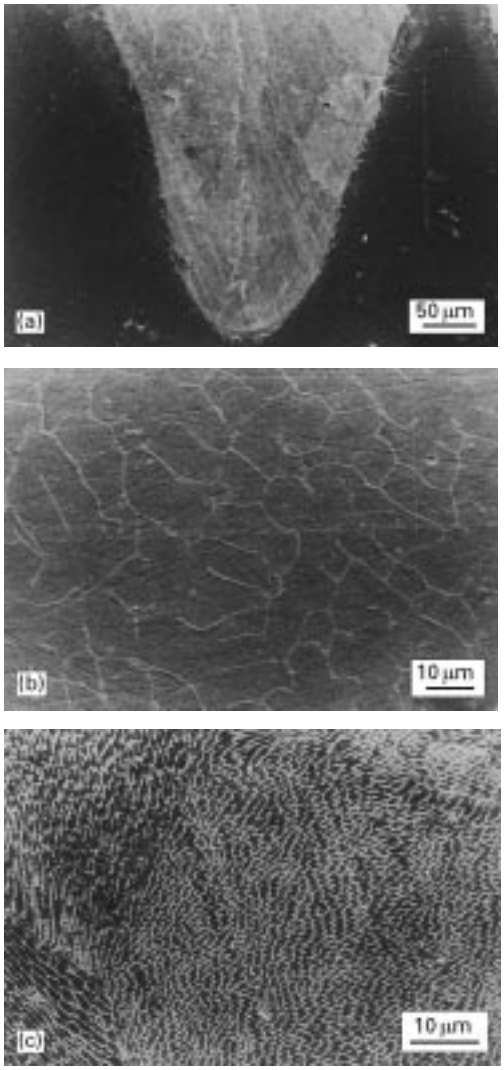

Figure 4 Secondary-electron images of an electron beam melted zone of Cu–80 wt % Co: (a) an overall view; (b) substrate near the fusion line; (c) molten pool.

0.5 mm, spherulites similar to those shown in Fig. 9a were observed, in which the particles near the splat face were fine, becoming coarser with increasing distance from the splat. As the thickness, D, increased to $0.5\,\text{mm} < D < 0.7\,\text{mm}$ (Fig. 9b), the microstructure at the midregion changed to dendritic. However, coarser spherical particles than those at the bottom were observed at the upper surface. For samples thicker than 0.7 mm (Fig. 9c), the bottom section consisted of fine spherulites, which gradually changed to regular Co dendrites far from the copper chill. The dendrites at the sample top surface were generally much coarser than those in the centre of the thinner samples (compare Fig. 9e with Fig. 9f). If, however, the sample was supercooled below the miscibility gap, the entire sample cross-section consisted of spherical particles, fine at the bottom and coarse at the centre, as shown in Fig. 9c, and by a higher magnification in Fig. 9d.

4. Discussion

4.1. Microstructure of electron beam surface-melted specimens

The microstructure of the electron beam fused zone for Cu–Co alloys containing less than 40 wt % Co consists of tiny spheres embedded in a matrix. The appearance of spherulites of one composition in a matrix of another composition implies that liquid-phase separation occurred prior to solidification [10]. As was found in previous work [10, 13, 15], bulk supercooling of alloys which undergo liquid-phase separation below a certain temperature, T_{SEP} resulted in the separation of the melt into two liquids; one poor in Cu, named L1, and a second rich in Cu, named L2. Each melt then solidifies on a path dictated by the stable phase diagram boundary. Usually, one liquid solidifies as spheres and the other as the matrix. Because of the short solidification time and the large convection involved in electron beam surface melting, the spheres have a small diameter, such as those appearing in Fig. 1e and f.

The solidification of electron beam surface-melted specimens is rather complicated, as thermal gradients across the interface change during solidification of the molten pool. At the beginning of solidification, the thermal gradient, G, is very large, and the interface velocity, R, is very small. Thus, the ratio G/R is very large. According to constitutional supercooling and morphological stability criteria [22], the condition for plane front solidification thus exists. As solidification proceeds, the thermal gradient decreases while the interface velocity increases. Thus, the G/R ratio decreases markedly, and solidification changes into a cellular solidification mode, which eventually turns to dendritic. The microstructural analysis shows that these transitions take place approximately 5–20 μm from the fusion line. In addition, it has been shown that the dendritic morphology changes to a two-melt microstructure (namely, Co-rich spheres embedded in a Cu-rich melt). These three morphological changes can be observed in Fig. 2c and d.

As proposed in our previous publication [10], considerable dynamic supercooling could take place up to a level of 150 K because the heat transport is larger than the mass transport. Such high supercooling levels might cause melt separation (i.e., Co-rich spheres embedded in a Cu-rich melt). Based on the metastable phase boundary [10], a minimum supercooling of 100 K is necessary for Cu–30 wt % Co to enter the immiscibility zone. As such, the regions ahead of the dendritic zone must have been supercooled by at least this amount.

It is conceivable that high cooling rates could lead to supercooling of the liquid ahead of an advancing interface if the interfacial kinetics are sluggish. For simple liquids such as Cu–Co, it is, however, unlikely that interfacial kinetics limitation alone could lead to such large supercoolings. Convective flow within a inhomogeneous liquid pool, on the other hand, could lead to a large bulk supercooling without requiring large interfacial supercooling. As shown in Fig. 2c, unmelted Co particles appeared at the fusion line, indicating that the liquid in this region had lower Co concentration than the original alloy, or to the well-mixed liquid in the middle of the pool. In fact, the fusion line is at the peritectic temperature where solidification starts after the beam passage. Since the rate of heat transfer is much faster than the mass transfer,

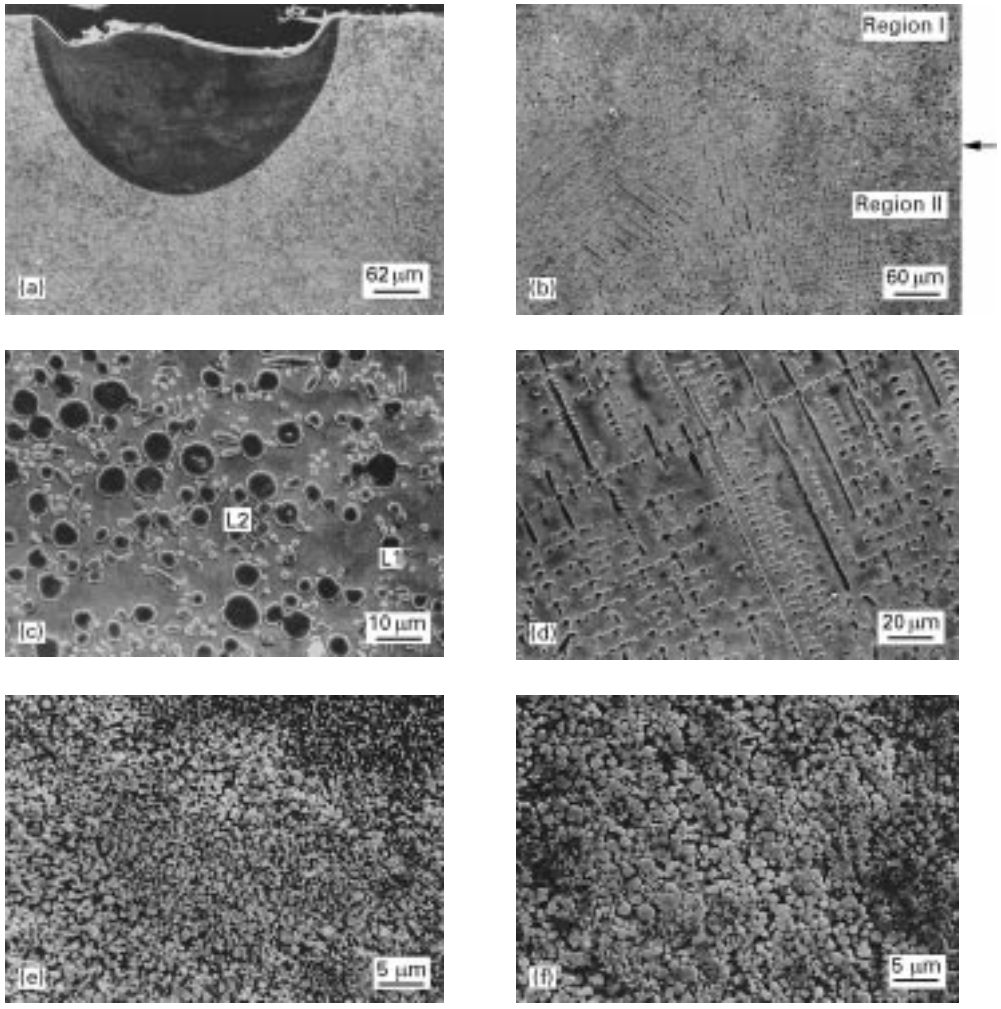

Figure 5 Secondary-electron images illustrating an electron beam melted surface of an arc-melted Cu–15 wt % Fe–10 wt % Co alloy: (a) overall view of the substrate and the melted surface; (b) microstructure at a low magnification; (c) higher magnification of the arc-melted substrate near the copper chill, demonstrating melt separation; (d) the microstructure far from the copper chill; (e) microstructure of the fused zone near the fusion line; (f) microstructure far from the fusion line.

the liquid pool temperature becomes more uniform before the liquid has sufficient time to homogenize. Under such conditions, portions of the liquid having large Co concentrations can constitutionally supercool before solidification starts. This dynamic supercooling, which results from compositional inhomogeneity, will be further enhanced as convective currents bring Co-rich liquid bands to the cooler parts near the fusion lines, are seen in Figs. 1c and 2e and f.

Electron beam surface melting of Cu–80 wt % Co alloys showed no evidence of melt separation. The process only caused microstructural refinement and increased Cu segregation, as evidenced by the relatively larger amount of interdendritic segregation. For that composition, more than 300 K supercooling is required to enter the miscibility gap, but these levels have not been achieved during the process.

4.2. Effect of cooling rate on the microstructure

Generally, as the cooling rates become higher, the solidification time becomes shorter, and the microstructure becomes finer. A similar effect is expected concerning the size of the phase-separated droplets solidifying in the metastable immiscibility zone. The cooling rates are the largest, and thus the coarsening times are shortest near the copper chill. Therefore, the spherulites near the copper chill are expected to be smaller than those far away from it, as seen in Fig. 9c.

According to the metastable liquid miscibility gap [10], the liquid must be supercooled by about 140 and 100 K to obtain liquid-phase separation in alloys containing 10 wt % Co and 30 wt % Co, respectively. The presence of fine spherulites in the fused zone of electron beam surface-melted alloys (Figs 1 and 2) is indicative that the high cooling rates cause supercooling levels beyond these values. Therefore, both high cooling rates and supercooling exist during electron beam surface melting.

The present work further indicates that large bulk supercooling might be obtained even under smaller cooling rates than those involved in electron beam surface melting, e.g., during splat quenching on a copper plate. As can be seen in Fig. 5b, melt separation was observed in certain Cu–Fe–Co alloys up to about 200 μm from the copper chill. This indicates that dynamic bulk supercooling was obtained for the arc-melted samples near the Cu chill. Furthermore, as described in Figs 8 and 9, a dominant factor

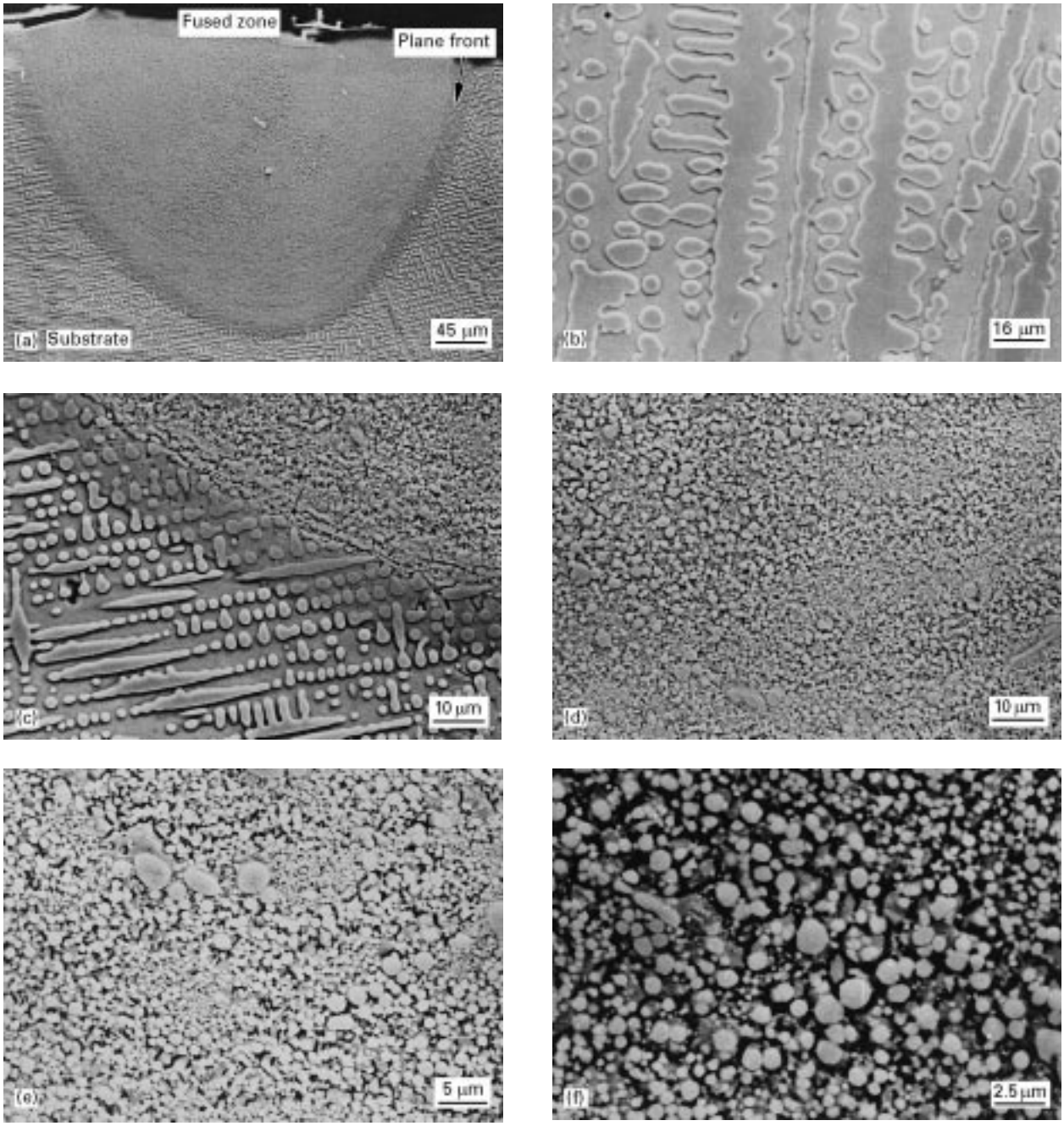

Figure 6 Secondary-electron images illustrating an electron beam melted surface of an arc-melted Cu–15 wt % Fe–10 wt % Co alloy: (a) overall view; (b) arc-melted microstructure; (c) higher magnification of electron beam fused path and vicinity; (d), (e) microstructure of the fused zone near the fusion line at two magnifications; (f) microstructure of the fused zone far from fusion line.

controlling the microstructure is the cooling rates, which depend on the sample thickness. In Cu–20 wt% Co specimens, with thickness less than 0.5 mm, which were splat quenched from 90 K supercooling, the entire microstructure consisted of fine spherulites (Fig. 8a). This indicates that an additional supercooling of at least 50 K was obtained prior to the nucleation. According to calculations by Abbaschian and Flemings [23], during the fall of a molten Fe–15 wt % Ni in the electromagnetic levitation apparatus one may expect sample cooling of about 15 K. Thus, it can be concluded that additional supercooling of at least 35 K was effected by the contact with the copper chill. Following Clyne [11], the bulk supercooling depends on the distance from the copper chill. Indeed, when the sample thickness is between 0.5 and 0.7 mm, spherulites could be observed only near the copper chill plate, as shown in Fig. 8b. Since this particular sample was dropped from a 160 K supercooling, it had already entered the miscibility gap prior to making the contact with the chill. The appearance of the large spherulites in the microstructure indeed indicates that the melt had already separated into two liquids and had sufficient time for coarsening before making contact with the chill. Even so, when the melt contacts the chill, it experiences additional supercooling, which in turn causes the already-separated L2 melt to undergo a secondary melt separation, as evidenced by the formation of finer spherulites. It should be noted that, upon nucleation and growth, initiated most probably at the contact with the chill, recalescence will take place. This raises the temperature of the remaining

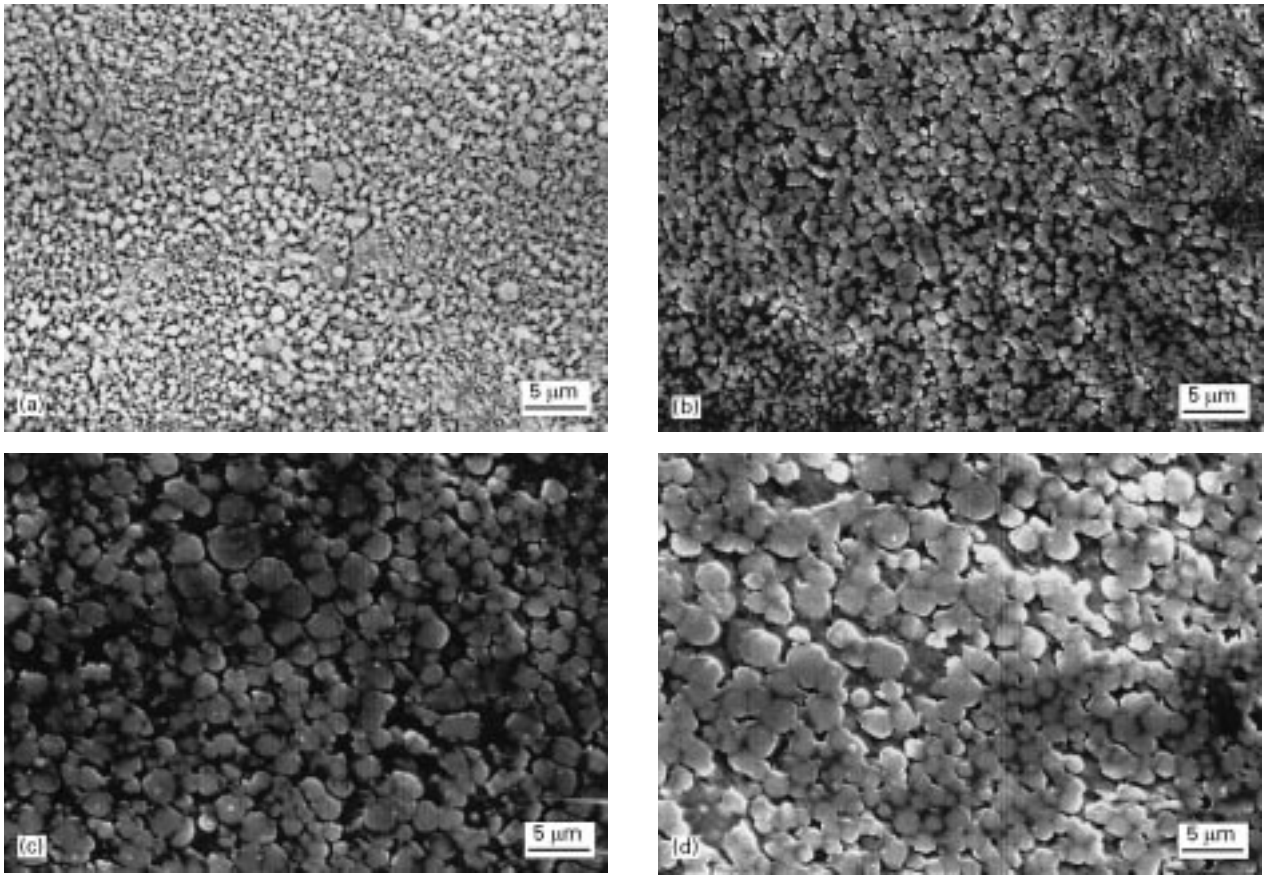

Figure 7 Secondary-electron images illustrating an electron beam melted surface of arc-melted Cu–Fe Co alloys as a function of the Fe + Co concentration: (a) Cu–15 wt % Fe–5 wt % Co; (b) Cu–15 wt % Fe–10 wt % Co; (c) Cu–25 wt % Fe–20 wt % Co; (d) Cu–40 wt % Fe–15 wt % Co.

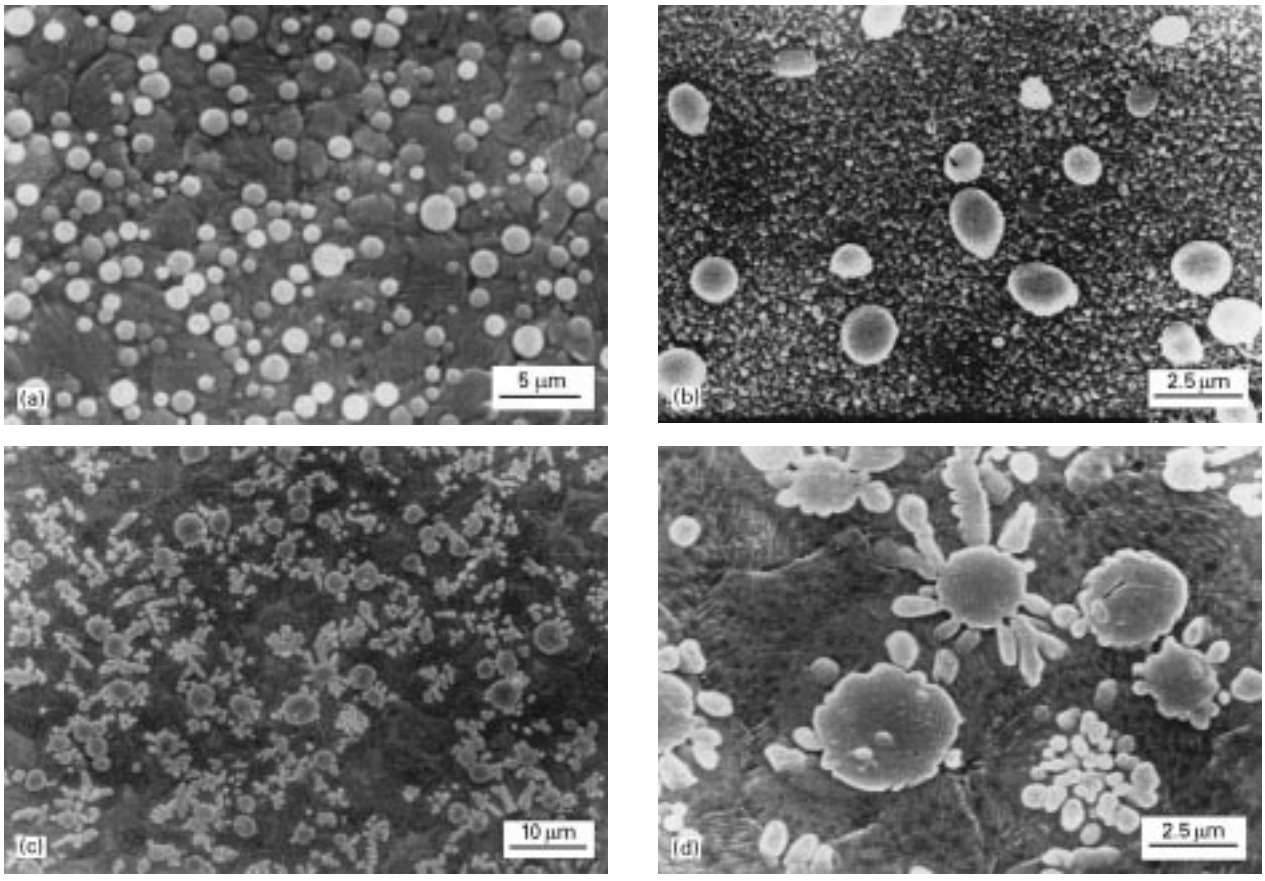

Figure 8 Secondary-electron images demonstrating the microstructure of Cu–20 wt % Co dropped on a copper chill for different supercoolings and distances from the chill: (a) 90 K supercooling 40 μm from the chill; (b) 160 K supercooling 10 μm from the chill; (c) 160 K supercooling 60 μm from the chill; (d) 160 K supercooling 80 μm from the chill.

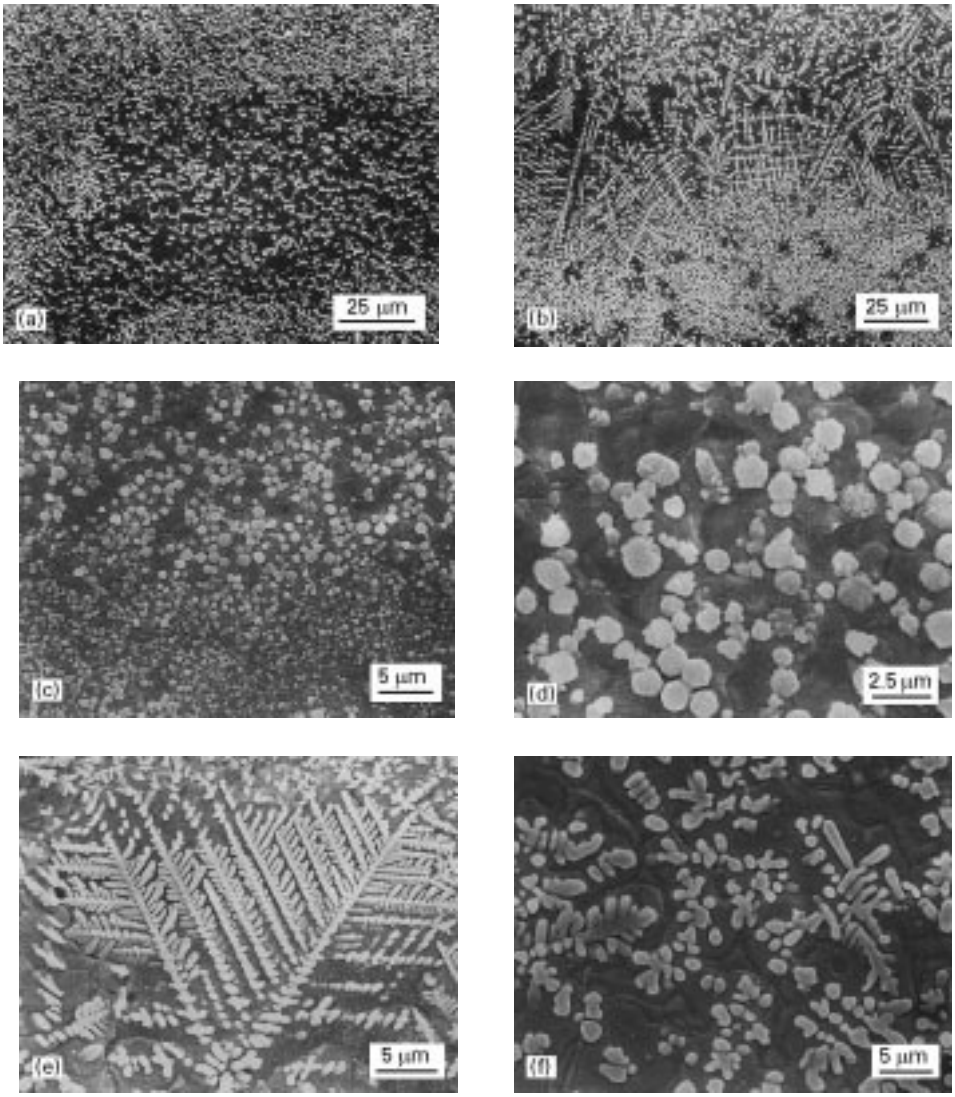

Figure 9 The microstructure change in Cu–20 wt % Co specimens for different sample thicknesses, D, and different supercoolings, ΔT: (a) $D < 0.5$ mm and $\Delta T = 100$ K before quenching; (b) $0.5 < D < 0.7$ mm and $\Delta T = 100$ K; (c) $\Delta T = 150$ K at sample centre; (d) $\Delta T = 150$ K at the sample top; (e) $D \approx 0.7$–0.9 mm at the sample centre; (f) $D \approx 0.7$–0.9 mm at the sample top.

liquid, thereby eliminating a portion of, if not all, the supercooling of the remaining liquid. A similar behaviour has been predicted by Clyne's [11] theoretical calculations. Thus, secondary-phase separation may not be seen in the upper parts of the samples.

5. Conclusions

The microstructures of binary Cu–Co alloys containing 10–80 wt % Co, and ternary Cu–Fe–Co alloys, solidified under high cooling rates were investigated, yielding the following results.

1. High cooling rates obtained by electron beam surface melting of Cu–Co and Cu–Fe–Co alloys containing Fe + Co concentrations less than 45 wt % caused metastable liquid separation into two liquids: one Cu poor (L1), and the other Cu rich (L2). This indicates a dynamic bulk supercooling of at least 150 K. The microstructure of the phase separated samples consisted of tiny spherulites of one liquid, embedded in a matrix of the other. The size of a spherulite increases with increasing Fe + Co concentration in the melt.

2. Supercooling of Cu–50 wt % Co causes a duplex structure of fine and coarse dendrites, without any clear liquid-phase separation boundaries.

3. Supercooling of Cu–80 wt % Co and Cu–Fe–Co alloys containing more than 55 wt % Fe + Co caused refinement of the dendritic structure, and increased the Cu solubility inside the Fe (Co) dendrites.

4. Similar metastable phase separation characteristics were observed in copper-quenched samples of Cu–Co and Cu–Fe–Co alloys near the splat surface.

Acknowledgements

The authors wish to thank C. Cotler for his technical assistance and Z. Barkai for his help with the SEM.

References

1. H. JONES, *Aluminum* **54** (1978) 274.
2. B. P. BARDES and M. C. FLEMINGS, *Trans. Amer Foundrymens' Soc.* **74** (1966) 406.

3. H. KANCKO and J. LKEUCHI, in Proceedings of the first International Conference on Electro-discharge Machining, Tokyo, 1965 (1965) p. 23.
4. P. RAMACHANDRARAO and M. LARIDJANI, *J. Mater. Sci.* **9** (1974) 434.
5. R. BUSCH, F. GARTNER, C. BORCHERS, P. HAASEN and R. BORMANN, *Acta Mater.* **44** (1996) 2567.
6. J. WECKER, R. VON HELMOLT and L. SCHULTZ, *Appl. Phys. Lett.* **62** (1993) 1985.
7. A. E. BERKOWITZ, J. R. MITCHELL, M. J. CAREY, A. P. YYOUNG, S. ZHANG, F. E. SPADA, F. T. PARKER, A. HUTTEN and G. G. THOMAS, *Phys. Rev. Lett.* **68** (1992) 3749.
8. J. Q. XIAO, J. S. JIANG and C. L. CHIEN, *Phys. Rev. Lett.* **68** (1992) 3745.
9. I. S. MIROSHNICHENKO and G. P. BREKHARYA, *Fiz. Metall. Metolloved.* **29** (1970) 664.
10. A. MUNITZ, S. P. ELDER and R. ABBASCHIAN, *Metall. Trans. A* **23** (1992) 1817.
11. T. W. CLYNE, *Metall. Trans. B* **15** (1983) 369.
12. W. J. BOETTINGER, S. R. CORIELL and R. F. SEKERKA, in "Chemistry and physics of rapidly solidified materials", edited by B. J. Berkowitz and R. O. Scattergood (Metallurgical Society of AIME, Warrendale, PA, 1982) p. 45.
13. A. MUNITZ and R. ABBASCHIAN, in " Undercooled alloy phases", edited by C. C. Koch and E. W. Collings (Metallurgical Society of AIME, Warrendale, PA 1987) p. 23.
14. S. P. ELDER, A. MUNITZ and R. ABBASCHIAN, *Mater. Sci. Forum* **50** (1989) 137.
15. A. MUNITZ and R. ABBASCHIAN, *J. Mater. Sci.* **26** (1991) 6458.
16. S. P. ELDER, PhD dissertation, University of Florida (1990).
17. Y. NAKAGAWA, *Acta Metall.* **6** (1958) 704.
18. T. NISHIZAWA and K. ISHIDA, *Bull. Alloy Phase Diagrams* **5** (1984) 161.
19. H. JONES, *Treatise Mater. Sci. Technol.* **20** (1981) 1.
20. R. MEHRABIAN, *Inter. Metals Rev.* **27** (1982) 185.
21. S. J. B. REED, "Electron microprobe analysis", (Cambridge University Press, Cambridge, Cambs., 1977) pp. 175–197.
22. W. A. TILLER, K. A. JACKSON, J. W. RUTTER and B. CHALMERS, *Acta Metall.* **1** (1953) 428.
23. G. J. ABBASCHIAN and M. C. FLEMINGS, *Metall. Trans. A*, **14** (1983) 1147.

Received 9 May 1997
and accepted 11 May 1998